

Article

Sulfur-Resistant CeO₂-Supported Pt Catalyst for Waste-to-Hydrogen: Effect of Catalyst Synthesis Method

Ga-Ram Hong¹, Kyoung-Jin Kim¹, Seon-Yong Ahn¹, Beom-Jun Kim¹, Ho-Ryong Park¹, Yeol-Lim Lee² , Sang Soo Lee¹ , Yukwon Jeon¹ and Hyun-Seog Roh^{1,*} 

¹ Department of Environmental and Energy Engineering, Yonsei University, 1 Yonseidae-gil, Wonju 26493, Republic of Korea

² Department of Chemical Engineering, Keimyung University, 1095 Dalgubeol-daero, Dalseo-gu, Daegu 42601, Republic of Korea

* Correspondence: hsroh@yonsei.ac.kr

Abstract: To improve the sulfur tolerance of CeO₂-supported Pt catalysts for water gas shift (WGS) using waste-derived synthesis gas, we investigated the effect of synthesis methods on the physico-chemical properties of the catalysts. The Pt catalysts using CeO₂ as a support were synthesized in various pathways (i.e., incipient wetness impregnation, sol-gel, hydrothermal, and co-precipitation methods). The prepared samples were then evaluated in the WGS reaction with 500 ppm H₂S. Among the prepared catalysts, the Pt-based catalyst prepared by incipient wetness impregnation showed the highest catalytic activity and sulfur tolerance due to the standout factors such as a high oxygen-storage capacity and active metal dispersion. The active metal dispersion and oxygen-storage capacity of the catalyst showed a correlation with the catalytic performance and the sulfur tolerance.

Keywords: waste-to-hydrogen; water-gas shift reaction; sulfur tolerance; synthesis method; oxygen-storage capacity; Pt⁰ dispersion



Citation: Hong, G.-R.; Kim, K.-J.; Ahn, S.-Y.; Kim, B.-J.; Park, H.-R.; Lee, Y.-L.; Lee, S.S.; Jeon, Y.; Roh, H.-S. Sulfur-Resistant CeO₂-Supported Pt Catalyst for Waste-to-Hydrogen: Effect of Catalyst Synthesis Method. *Catalysts* **2022**, *12*, 1670. <https://doi.org/10.3390/catal12121670>

Academic Editor: Rufino Navarro Yerga

Received: 18 November 2022

Accepted: 16 December 2022

Published: 19 December 2022

Publisher's Note: MDPI stays neutral with regard to jurisdictional claims in published maps and institutional affiliations.

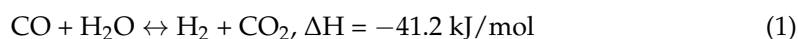


Copyright: © 2022 by the authors. Licensee MDPI, Basel, Switzerland. This article is an open access article distributed under the terms and conditions of the Creative Commons Attribution (CC BY) license (<https://creativecommons.org/licenses/by/4.0/>).

1. Introduction

Environmental policies and research worldwide recently aimed to achieve carbon neutrality (net-zero) by 2050. This is because 55% of the world's population lives in urban areas, and this proportion is expected to increase to 68% by 2050, leading to rapid urbanization. Furthermore, the world's present population is predicted to increase by 30%, leading to serious overuse of energy and global warming [1]. Therefore, replacing fossil fuels with more environmentally-friendly fuels has received more attention in recent years due to relevant environmental issues and an increasing energy demand. In particular, sustainable renewable energy such as hydrogen is a key factor for achieving net-zero [2].

Hydrogen is considered the most preferred alternative energy because of its numerous advantages, such as zero pollution, sustainability, and ease of storage [3]. However, more than 96% of hydrogen is produced using fossil fuels as a source [3,4]. As an alternative to this, the process of producing hydrogen from various waste resources is being actively studied [2,5,6]. As one primary type of waste, municipal solid waste has great interest worldwide [3,7–9]. Municipal solid waste is converted into useful syngas composed of CO and H₂ through the waste gasification process, which is one of the representative technologies of waste-to-energy [2,10,11]. By applying a water-gas shift (WGS) reaction (Equation (1)), the waste-derived synthesis gas can be converted into hydrogen [11–13].



Here, the considerations in applying waste-derived synthesis gas to WGS are different from that in applying the conventional synthesis gas from natural gas. Waste-derived synthesis gas is mainly composed of CO (>38%) [10,11] with a trace amount of sulfur

components [14,15]. Therefore, in the design of high-performance WGS catalysts for hydrogen production from waste-derived synthesis gas, it is essential to ensure high CO conversion in excessive CO conditions and sulfur resistance. Since trace amounts of sulfur components are preferentially adsorbed into the active sites of the catalysts to cause rapid deactivation, understanding the correlation between the physicochemical properties of the catalysts and sulfur resistance is emerging as a major research issue [15,16].

Previously, we confirmed that a Pt catalyst using CeO₂ as a support exhibited excellent catalytic activity and sulfur resistance in WGS reactions using synthesis gas from waste-containing sulfur components [17]. The optimal amount of Pt loading was then found to enhance the performance of the catalyst [18]. CeO₂ is an excellent reducible support as an oxygen buffer that can greatly enhance the reaction rates involving redox steps in the WGS reactions [19,20]. It has been widely reported that CeO₂ is easily and reversibly reduced to several CeO_{2-x} stoichiometries when exposed to an oxygen-deficient atmosphere [20]. This unique characteristic of CeO₂ results in a high oxygen-storage capacity (OSC). In addition, the presence of Pt can weaken the Ce–O bond, changing the surface properties, which makes the surface CeO₂ more reducible [21,22]. These reduction properties in the CeO₂-PtO_x interfaces are explained by the oxygen reverse spillover phenomenon from CeO₂ [21,23]. Due to this synergistic effect, the Pt/CeO₂ catalyst has recently been actively studied as a catalyst for the WGS reaction [24–27].

In the catalyst optimization process, the synthesis method is an important consideration that can improve catalytic performance [28–31]. As reported by Zhang et al., the Au/CeO₂ catalyst prepared by the incipient wetness impregnation (IWI) method for the CO oxidation reaction was compared with the catalyst prepared by the deposition-precipitation method [28]. The catalyst prepared by the IWI method showed excellent catalytic activity by forming smaller and more uniform gold particles on the catalyst surface. Kim et al. reported that the CeO₂-supported Co catalyst prepared by the sol-gel (SG) method showed excellent WGS activity due to the high concentration of oxygen vacancies originating from the strong metal–support interaction [29]. Li et al. prepared CeO₂-MoO₃ catalysts by various synthesis methods for the selective catalytic reduction of NO with NH₃ [30]. They claimed that catalysts prepared by the hydrothermal (HT) method showed a larger surface area, highly dispersed nanocrystalline CeO₂, good redox ability, and stronger adsorption capacity. Lee et al. prepared catalysts by co-precipitation (CP), IWI, HT, co-impregnation, and sequential impregnation methods for dry reforming using coke oven gas [31]. The catalyst prepared by CP showed improved catalytic performance, which was due to the strong metal–support interaction. Considering the above results, it can be confirmed that the physicochemical properties of the catalyst change according to the synthesis methods. Therefore, the synthesis method is an important factor influencing catalyst performance. In this study, the effect of the synthesis method on the physicochemical properties of the catalyst was investigated by varying the synthesis method (IWI, SG, HT, and CP) of the CeO₂-supported Pt catalysts. The factors that improve the catalytic activity and sulfur tolerance in the WGS reaction were investigated, and an optimal synthesis method was derived. The prepared catalysts by various synthesis methods (IWI, SG, HT, and CP) were denoted as PtCe-I, PtCe-S, PtCe-H, and PtCe-C, respectively.

2. Results and Discussion

The XRD patterns for CeO₂-supported Pt catalysts prepared by various synthesis methods are shown in Figure 1. The patterns of all prepared samples exhibited peaks attributable to the face-centered cubic fluorite structure of CeO₂ (JCPDS No. 34-0394) [32]. In the case of the PtCe-H and PtCe-C catalysts, Pt (111) diffraction peaks were observed at a 2θ of 39.8° (JCPDS No. 04-0802) [33]. This indicates that the metal crystallites on the CeO₂ supports were either largely formed or have high crystallinity. Conversely, when using the PtCe-I and PtCe-S catalysts, clear diffraction peaks of Pt nanoparticles were not observed because they are small and well dispersed over the support. The improved dispersion has a positive effect on enhancing the catalytic activity for the WGS reaction [20,34].

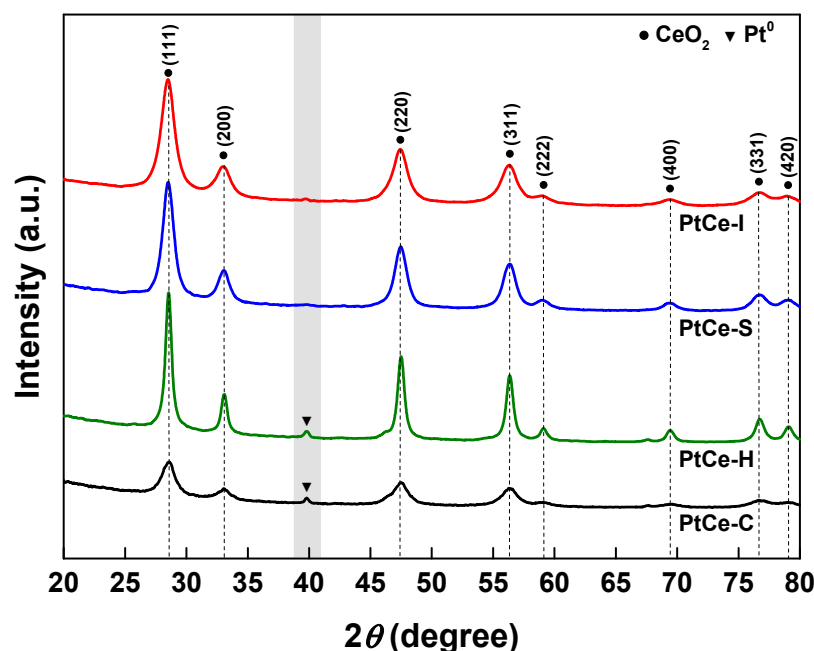


Figure 1. XRD patterns of reduced CeO_2 -supported Pt catalysts prepared by various synthesis methods.

Table 1 summarizes the physicochemical properties of PtCe catalysts prepared by various synthesis methods. The specific surface area of the samples shows the following order: PtCe-C ($132 \text{ m}^2/\text{g}$) > PtCe-I ($107 \text{ m}^2/\text{g}$) > PtCe-H ($78 \text{ m}^2/\text{g}$) > PtCe-S ($67 \text{ m}^2/\text{g}$). Figure S1 shows the N_2 adsorption–desorption isotherms of PtCe catalysts prepared by various synthesis methods. All the catalysts presented a type IV isotherm with a hysteresis loop, which indicates the mesoporous capillary condensation. According to the IUPAC classification, PtCe-I and PtCe-H exhibited an H1 hysteresis loop [35,36]. H1 hysteresis indicates the presence of cylindrical pores having a uniform size or shape. PtCe-S exhibited an H3 hysteresis loop type, whereas PtCe-C exhibited an H2 hysteresis loop type [35,37]. Figure S2 shows the pore distribution of PtCe catalysts prepared by various synthesis methods. As discussed for the isotherms, the PtCe-I catalyst exhibited mesopore distribution. The PtCe-H catalyst contained mesopores and even macropores. The PtCe-S catalyst showed a non-uniform distribution of pores with mesopores close to micropores and up to macro pores. The PtCe-C catalyst showed a distribution of relatively small-sized mesopores compared to the PtCe-I catalyst.

Table 1. Physicochemical properties of CeO_2 -supported Pt catalysts prepared by various synthesis methods.

Catalyst	S.A. (m^2/g) ^a	Pore Volume (cm^3/g) ^a	Pt ⁰ Dispersion (%) ^b	Pt ⁰ Particle Size (nm) ^b	H ₂ Consumption (mmol/g) ^c
PtCe-I	107	0.415	89.9	1.05	8.29
PtCe-S	67	0.216	53.4	1.77	5.47
PtCe-H	78	0.357	36.2	2.60	3.52
PtCe-C	132	0.308	2.4	39.3	6.23

^a Estimated by N_2 -adsorption/desorption at $-196 \text{ }^\circ\text{C}$; ^b Estimated from CO -chemisorption; ^c Estimated from H_2 -TPR analysis.

Synthesis methods changed the specific surface area as well as the Pt⁰ dispersion. As confirmed by CO chemisorption analysis, the PtCe-I catalyst showed the highest value of 89.9% and the PtCe-C catalyst showed the lowest value of 2.4%. The PtCe-S and PtCe-H catalysts showed a Pt⁰ dispersion of 53.4% and 36.2%, respectively. Metal dispersion is generally defined as the ratio of the number of active sites exposed on the catalyst surface,

and only the atoms exposed on the surface can participate in the catalyst surface reaction. In the WGS reaction, the CO_2 product generates through the adsorption of CO on the active Pt particles of the catalyst surface during the reaction process [21]. Therefore, it is expected that the PtCe-I catalyst with the highest Pt^0 dispersion would show high WGS activity.

Concerning H_2 -TPR (Figure 2), two peaks related to the redox properties of the CeO_2 -supported Pt catalysts were observed. During the reduction process, the first intense peak centered at low temperatures ($<200\text{ }^\circ\text{C}$) included the reduction of oxidized Pt species, as well as partial reduction of O species between Pt nanoparticles and CeO_2 interfaces [21,38,39]. The second peak located at high temperatures over $300\text{ }^\circ\text{C}$ is ascribed to the reduction of CeO_2 [28,38]. The reduction behaviors of the catalysts were clearly different depending on the catalyst synthesis method. The first reduction peak of the PtCe-I catalyst appeared at the lowest temperature among the tested samples. The reduction temperature of the catalytic active species ($\text{CeO}_2\text{-PtO}_x$) was as follows: PtCe-S ($181\text{ }^\circ\text{C}$) $>$ PtCe-C ($111\text{ }^\circ\text{C}$) $>$ PtCe-H ($93\text{ }^\circ\text{C}$) $>$ PtCe-I ($75\text{ }^\circ\text{C}$).

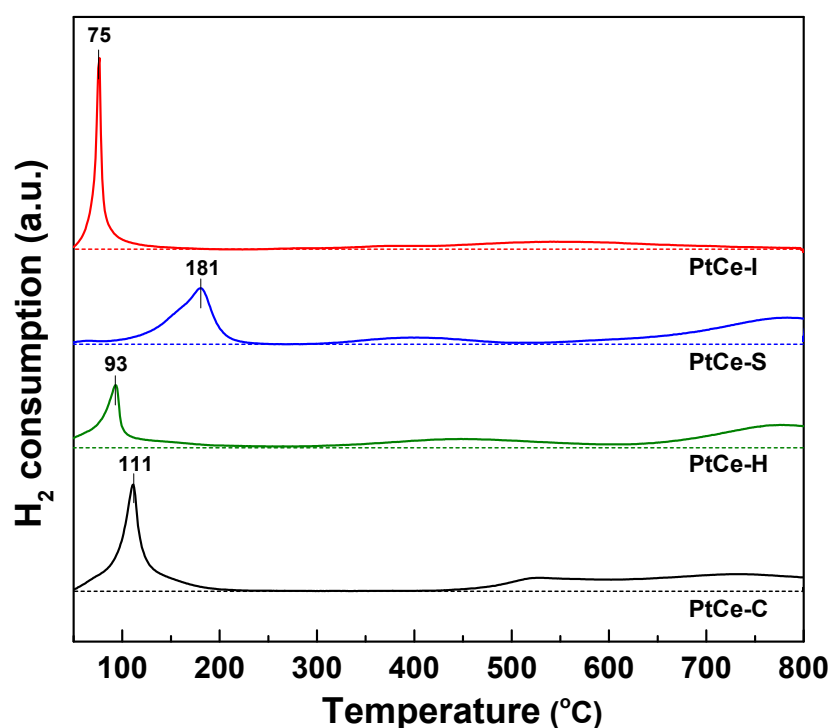


Figure 2. H_2 -TPR profiles of CeO_2 -supported Pt catalysts prepared by various synthesis methods.

To compare the reducibility of the catalyst in detail, the H_2 consumption of the catalyst was also calculated and is shown in Table 1. The hydrogen consumption of each catalyst was calculated with the first peak between 50 and $300\text{ }^\circ\text{C}$. The PtCe-I catalyst showed the highest H_2 consumption compared to the others. In addition, as the lattice oxygen of CeO_2 has reversely spilled over at lower temperatures, the second reduction peak area of the PtCe-I catalyst was markedly decreased [21,38]. The reduction behaviors of $\text{CeO}_2\text{-PtO}_x$ interfaces are related to the reaction between hydrogen and reversely spilled-over oxygen from CeO_2 [21,23,39]. According to the results of the above analysis, the oxygen reverse spillover amount of CeO_2 -supported Pt catalysts is different depending on the synthesis method. The oxygen reverse spillover further modifies the redox properties of CeO_2 -supported Pt catalysts [23,40]. The WGS reaction is widely known to operate through a redox mechanism in the high-temperature range [23,41]. In detail, CO is adsorbed to active sites and oxidized by mobile oxygen species on the catalysts [21]. Then, the defect oxygen sites are reoxidized by water adsorbed on the oxide surface and generate hydroxyl groups [40]. Therefore, the redox property of the catalyst is a main factor that affects

the activity of the WGS catalyst. Consequently, the PtCe-I catalyst with excellent redox properties and high H₂ consumption is expected to exhibit relatively high catalytic activity for the WGS.

To assess the surface electronic properties of the CeO₂-supported Pt catalysts, the reduced samples were analyzed by XPS (Figure 3). The reduction conditions were the same as the pretreatment (400 °C with 5% H₂/N₂) applied to the reaction. Figure 3A shows the XPS Pt 4f spectra of the CeO₂-supported Pt catalysts. Through the reduction process, PtO_x was reduced to metallic Pt⁰. The corresponding Pt⁰ peaks are displayed at 74.3 (Pt 4f_{5/2}) and 71.0 eV (Pt 4f_{7/2}) [42,43]. The PtCe-I and PtCe-S catalysts clearly showed Pt⁰ peaks. Conversely, the PtCe-H and the PtCe-C catalysts showed a weak Pt⁰ peak. It can be considered that Pt is not sufficiently exposed on the catalyst surface in the PtCe-H and PtCe-C catalysts [44]. This trend is consistent with the Pt dispersion results. This same result was also shown in the poisoned samples (Figure S3).

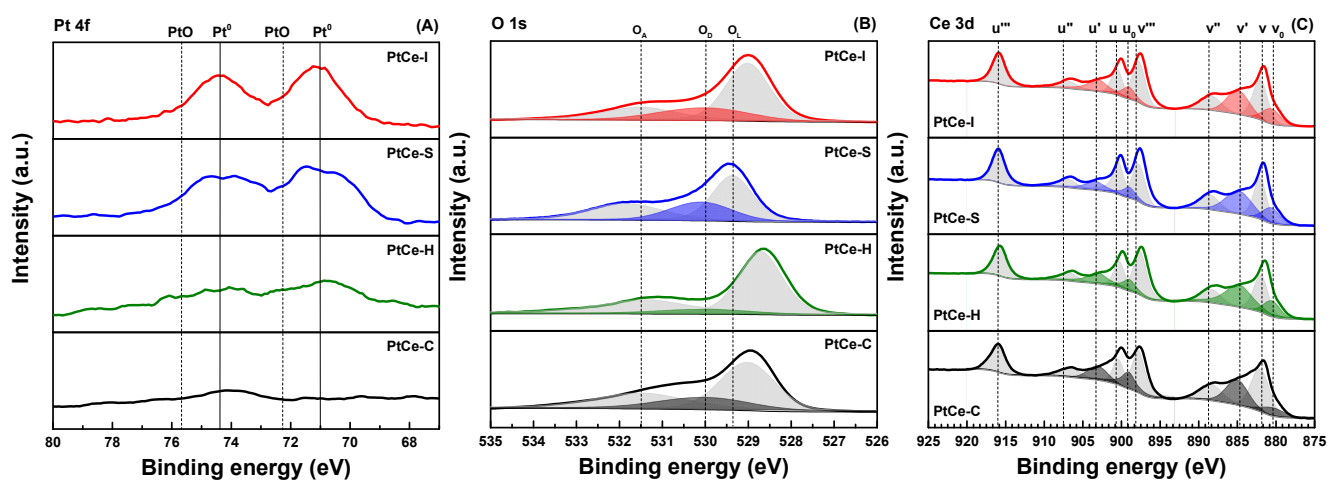


Figure 3. XPS spectra of reduced CeO₂-supported Pt catalysts prepared by various synthesis methods. (A) Pt 4f; (B) O 1s; (C) Ce 3d.

From the XPS analysis results, the O 1s and Ce 3d spectra can provide the surface concentration of oxygen vacancies. In the O 1s spectra (Figure 3B), the peaks deconvoluted into three main peaks: 529.4, 530, and 531.5 eV [45,46]. Each deconvoluted peak represents: 529.4 eV (lattice oxygen (O_L)); 530 eV (defect oxygen (O_D)); and 531.5 eV (adsorbed oxygen species (O_A)), respectively [45,46]. In particular, the oxygen vacancy value of the catalyst can be assumed through the O_D peak shown in color at 530 eV [46]. As the number of defect oxygen species in CeO₂ increases, the content of Ce³⁺ surface defects, leading to the formation of oxygen vacancies [47]. This oxygen vacancy serves as a site for mobile oxygen that participates in the redox mechanism of the WGS reaction, thereby accelerating the reaction [40]. It has been reported that the oxygen vacancy of the PtCe catalyst is related to the reduction of CeO₂ through oxygen reverse spillover [23,40]. Table 2 shows the surface atomic concentration of the O_D calculated from the deconvoluted results. The surface atomic concentration of O_D in the catalysts shows the order of PtCe-I (22.18%) > PtCe-C (18.31%) > PtCe-S (11.66%) > PtCe-H (10.35%). Thus, it is expected that the PtCe-I catalyst exhibits high activity.

Table 2. Oxygen-storage capacity-related values of CeO₂-supported Pt catalysts prepared by various synthesis methods.

Catalyst	O _D (%) ^a	Ce ³⁺ (%) ^b	OSC (10 ⁻⁴ gmol/g _{cat}) ^c
PtCe-I	22.18	32.21	4.68
PtCe-S	11.66	29.57	1.85
PtCe-H	10.35	28.19	1.45
PtCe-C	18.31	31.04	4.11

^a Estimated from XPS O 1s spectra. ^b Estimated from XPS Ce 3d spectra. ^c Estimated from the H₂-O₂ pulse reaction.

The Ce 3d spectra (Figure 3C) of the samples exhibited multiple peaks related to Ce³⁺ and Ce⁴⁺ at 882–916.4 eV. The peaks were deconvoluted into 10 peaks ($v_0, v, v', v'', v''', u_0, u', u, u'',$ and u''') from five doublets of the spin-orbit split, respectively [48,49]. Among the peaks, the two colored doublets ($v_0, u_0,$ and v', u') are related to Ce³⁺, which correspond to the states of Ce 3d⁹4f¹ O 2p⁶ and Ce 3d⁹4f² O 2p⁵, respectively [48]. The formation of Ce³⁺ ions is ascribable to the reduction of the CeO₂ support, indicating the generation of oxygen vacancies [50,51]. Specifically, the movement of mobile oxygen occurs at oxygen vacancies in the CeO₂ lattice of the catalyst [40]. Thus, the tendency of Ce³⁺ was expected to follow the trend of O_D. The ratio of Ce³⁺ was calculated by Equation (2) figure based on the deconvoluted XPS Ce 3d spectra.

$$\text{Ce}^{3+} (\%) = \left\{ (Av_0 + Av' + Au_0 + Au') / \sum Ai \right\} \times 100 \quad (2)$$

where $\sum Ai$ is the total area of the original Ce 3d peak before deconvolution. Table 2 displays the Ce³⁺ concentration values obtained in the calculation. As expected, the results followed the same trend as the O_D, in the order PtCe-I (32.21%) > PtCe-C (31.04%) > PtCe-S (29.57%) > PtCe-H (28.19%).

The OSC measurements of the catalysts were performed by an H₂-O₂ pulse reaction (Table 2). The OSC value of the catalysts provides information on the reactive and available oxygen atoms related to the WGS redox mechanism [20,41]. The OSC intimately relates to the sulfur tolerance of the catalyst according to previous studies [17,18]. The catalyst with the higher OSC showed high sulfur tolerance [17,18]. In particular, the CeO₂ support contributes to the redox reaction by providing mobile oxygen due to the unique characteristics (e.g., rich oxygen vacancies and ease of change between Ce³⁺ and Ce⁴⁺) to promote redox [19,50,52]. A platinum-based catalyst supported on a reducing oxide such as ceria can exhibit superior redox properties due to its high OSC [21]. This explained the generation of oxygen vacancies through oxygen reverse spillover according to previous reports [18,23]. The trend of the oxygen-storage capacity of PtCe catalysts showed the following order: PtCe-I (4.68 × 10⁻⁴ gmol/g_{cat}) > PtCe-C (4.11 × 10⁻⁴ gmol/g_{cat}) > PtCe-S (1.85 × 10⁻⁴ gmol/g_{cat}) > PtCe-H (1.45 × 10⁻⁴ gmol/g_{cat}). This result indicated that the oxygen-storage capacity of the catalyst can be changed by controlling the synthesis method. The PtCe-I catalyst exhibited the best redox properties which originated from the high OSC of the catalysts. This was demonstrated by showing the same trend in the H₂-TPR, XPS, and H₂-O₂ pulse reaction. Thus, the PtCe-I catalyst is expected to exhibit high WGS activity and sulfur resistance among the prepared samples.

To investigate the structural information about the lattice disorder and defects of the prepared catalysts, Raman spectroscopy was conducted, and the results are shown in Figure 4. In all cases, a band at approximately 460 cm⁻¹, corresponding to the F_{2g} triple degenerate vibrational mode of the fluorite structure (face-centered cubic) of the CeO₂, was observed [53,54]. Since this mode is very sensitive to the vibrations of oxygen around the Ce ions, changes in the state of Ce ions or oxygen lattice have a significant effect on this mode [55]. The peak of the corresponding mode changes to be broader and asymmetric due to the local structure distortion of CeO₂. This distortion causes defects in the CeO₂ structure, which are related to the oxygen vacancies. Thus, the broadening and asymmetry of the

main peak at 460 cm^{-1} are related to the oxygen vacancies in the CeO_2 structure [50,54,56]. The PtCe-I catalyst had a noticeably broadened peak, followed by the PtCe-C catalyst, which had a weak and broad peak. The PtCe-S and PtCe-H catalysts showed relatively sharp and clear peaks. This trend agreed with the OSC results in the XPS and $\text{H}_2\text{-O}_2$ pulse reaction.

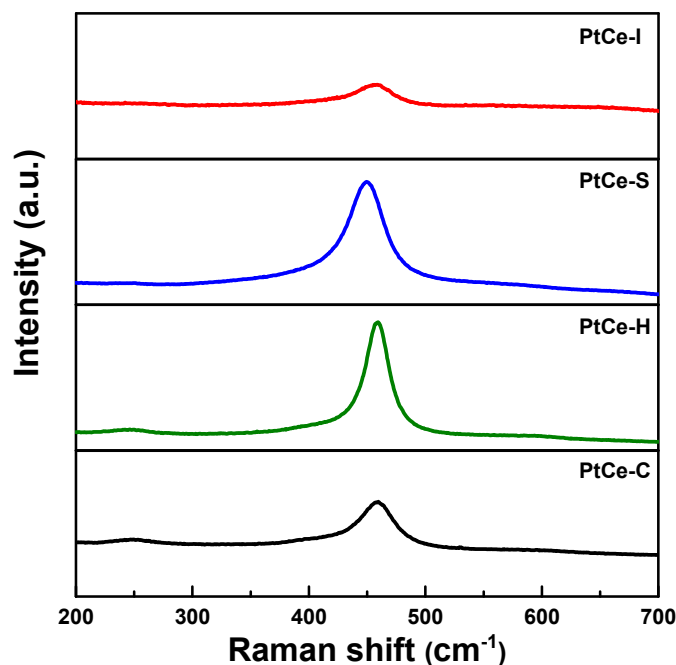


Figure 4. Raman spectra of reduced CeO_2 -supported Pt catalysts prepared by various synthesis methods.

Figure 5 shows the TEM images and EDS mapping results of all reduced samples. The extent and distribution of Pt species exposed on the surface varied according to the synthesis method. This suggests that the Pt dispersion is affected by the synthesis method, which is consistent with the trends in the CO-chemisorption (Table 1) and XPS results (Figure 3A). In addition, TEM images and particle size distribution results of reduced and poisoned CeO_2 -supported Pt catalysts are exhibited in Figure S4. The TEM images of all the reduced and poisoned catalysts showed a mixed morphology of particles with irregular shapes. It is difficult to clearly distinguish Pt particles in both the reduced and poisoned TEM images. The PtCe-I catalyst showed relatively smaller particle sizes compared to other catalysts.

As shown in Figure 6A, the CO conversion of the CeO_2 -supported Pt catalysts showed a clear difference depending on the synthesis method. Each catalyst was tested under two conditions, and the results are shown for each section. First, the intrinsic catalytic activity for the WGS reaction using waste-derived synthesis gas without sulfur components was confirmed. In the next step, the sulfur tolerance of the catalyst was evaluated for 100 h with an injection of H_2S (500 ppm). Sulfur contained in the feed gas is adsorbed on the catalyst surface and acts as a poison that decreases the catalyst activity [15,16]. As can be seen from TEM and EDS mapping images in Figure S5, sulfur was adsorbed to the catalyst. As expected from the characterization results, the PtCe-I catalyst exhibited the highest catalytic activity. In particular, the catalyst prepared by the impregnation method not only showed a high CO conversion of 90%, but also maintained a high catalytic activity without significant deactivation, even after sulfur injection. The PtCe-S catalyst exhibited the second highest intrinsic catalytic activity and sulfur tolerance. Conversely, the PtCe-H catalyst showed lower intrinsic catalytic activity than the previous two catalysts and was more rapidly deactivated in the presence of sulfur. In the case of PtCe-C catalyst, the lowest CO conversion was observed. Here, the intrinsic catalytic activity in sulfur-free condition

of the catalysts was most affected by Pt⁰ dispersion. The PtCe-I catalyst showed the highest Pt⁰ dispersion, followed by the PtCe-S and PtCe-H catalysts. However, the PtCe-C catalyst showed a remarkably low active species dispersion. This indicates that there are relatively few active species present on the catalyst surface that provide sites for the reaction. Thus, it can be considered that this result affects the lower catalytic performance. All other catalysts except the PtCe-C catalyst showed 100% CO₂ selectivity during the reaction (Figure 6B). On the other hand, the PtCe-C catalyst exhibited methanation ($\text{CO} + 3\text{H}_2 \rightarrow \text{CH}_4 + \text{H}_2\text{O}$), a major side reaction of the WGS reaction [57]. This is because the site for adsorption of the reactants was not sufficiently provided due to the remarkably low Pt dispersion of the PtCe-C catalyst. The numerical values related to the WGS reaction results of the catalysts are summarized in Table S1. To understand the intrinsic catalytic activity of the catalyst more clearly, turnover frequency (TOF) was calculated from the CO-chemisorption analysis and the WGS reaction results (Table 3). It is interesting that the PtCe-I catalyst exhibits similar TOF values to PtCe-S and PtCe-H catalysts, even when excluding the effect of Pt dispersion. This indicates that other catalytic properties such as OSC influence the intrinsic activity of CeO₂-supported Pt catalysts.

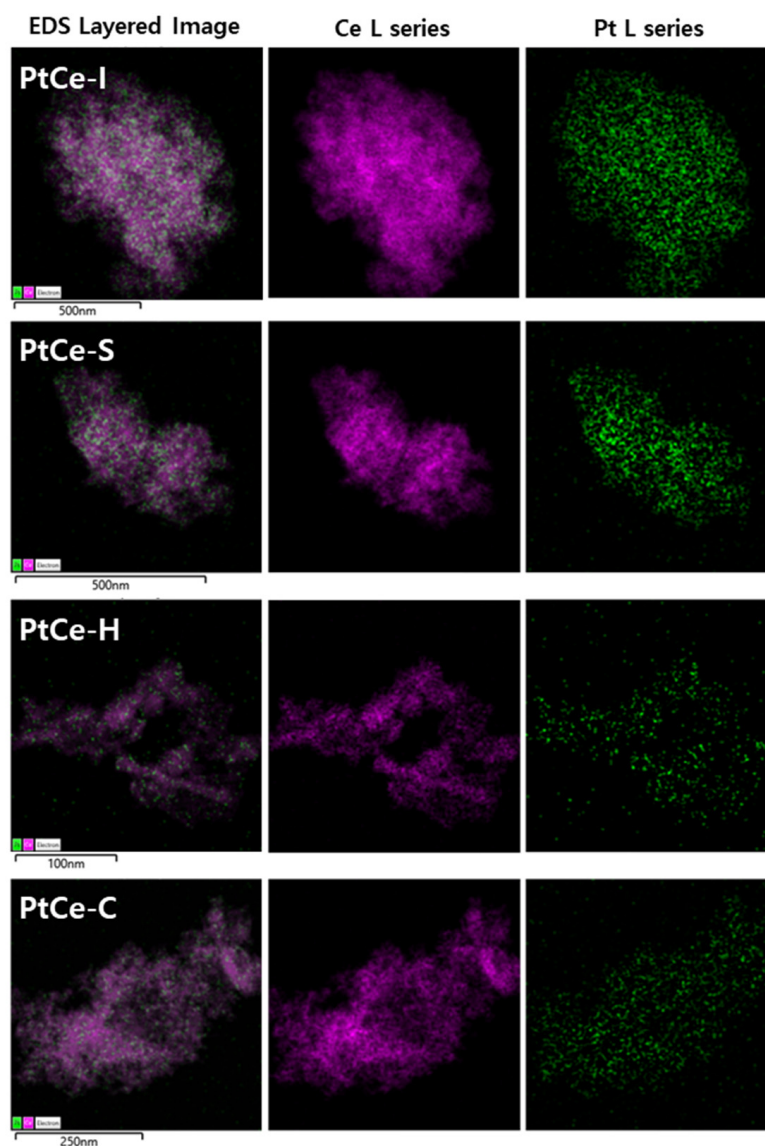


Figure 5. TEM images and EDS mapping results of reduced CeO₂-supported Pt catalysts prepared by various synthesis methods.

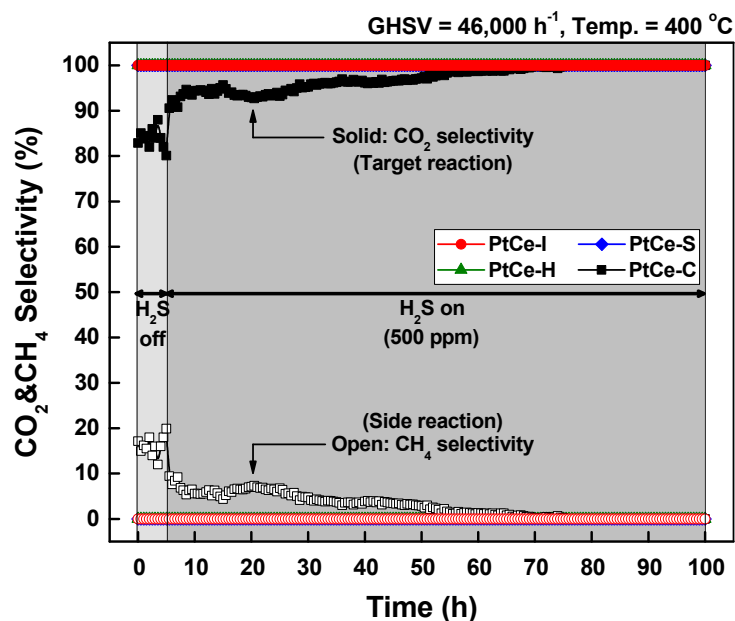
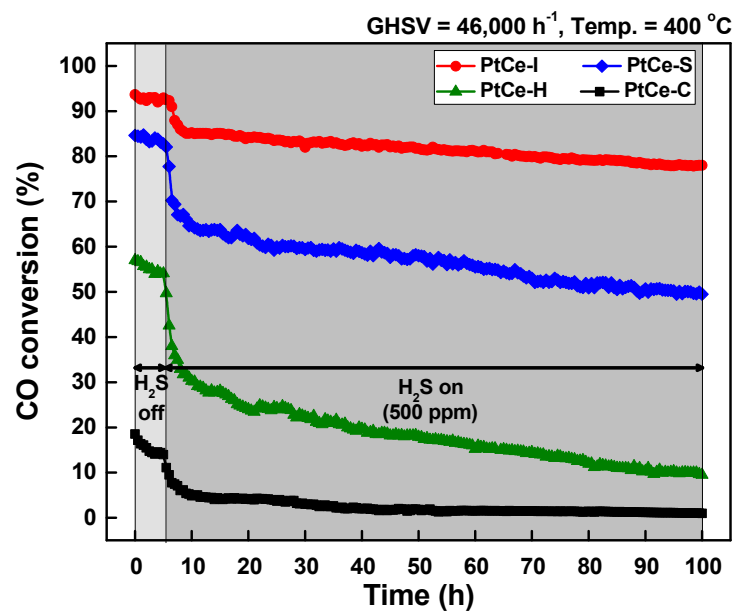


Figure 6. (A) CO conversion and (B) CO₂ and CH₄ selectivity as a function of time on stream over CeO₂-supported Pt catalysts prepared by various synthesis methods.

Table 3. Turnover frequency results over CeO₂-supported Pt catalysts prepared by various synthesis methods.

Catalyst	Turnover Frequency (s ⁻¹)
PtCe-I	0.010
PtCe-S	0.015
PtCe-H	0.015
PtCe-C	0.071

It has been previously reported that the OSC of the catalyst is a critical factor along with the dispersion of Pt in the WGS reaction [17,18]. In the WGS reaction, oxygen vacancies occurring as mobile oxygen in the lattice of CeO₂ oxidize the reactant CO to produce the product CO₂. Subsequently, oxygen is stored in the oxygen vacancies from H₂O dissociation. The higher the OSC value of the catalyst, the higher the retention of mobile oxygen that promotes the redox mechanism of the WGS reaction. Therefore, the high OSC value of the catalyst is related to excellent WGS reaction activity. Among the prepared samples, the PtCe-I catalyst exhibited the highest OSC value in the H₂-TPR, XPS (ratio of O_D and Ce³⁺), and H₂-O₂ pulse reaction. Additionally, it is reported that the mobile oxygen derived from CeO₂ reacts with the attached sulfurs on the active sites of the catalytic surface (S + mobile O → SO₂) and causes a regeneration of the catalytic performance [18]. Therefore, the OSC value is considered to be the most important factor in evaluating the sulfur tolerance of the catalysts. The PtCe-I catalyst showed the lowest activity loss and thus the highest sulfur tolerance. However, the PtCe-C catalyst showed low catalytic activity despite the relatively high OSC values. This is because the PtCe-C catalyst has a significantly lower number of activated Pt on the surface of the catalyst than that of the other catalysts, and thus the intrinsic activity of the catalyst is low. Nevertheless, OSC is an important factor in sulfur tolerance given the low decrease values of CO conversion in the PtCe-C catalyst. For this reason, the PtCe-I catalyst appears to exhibit high catalytic activity and superior sulfur tolerance due to the excellent redox properties and dispersion of the Pt active species on the catalytic surface.

The stability of the PtCe-I catalyst was further evaluated in sulfur-injection shutdown/re-start cycles (Figure 7). The cycle test was conducted 4 times in 100 h. The PtCe-I catalyst maintained high catalytic activity and sulfur resistance even during multiple poisoning and regeneration operations. Furthermore, it was shown that the catalytic activity of the catalyst was almost recovered at every cycle.

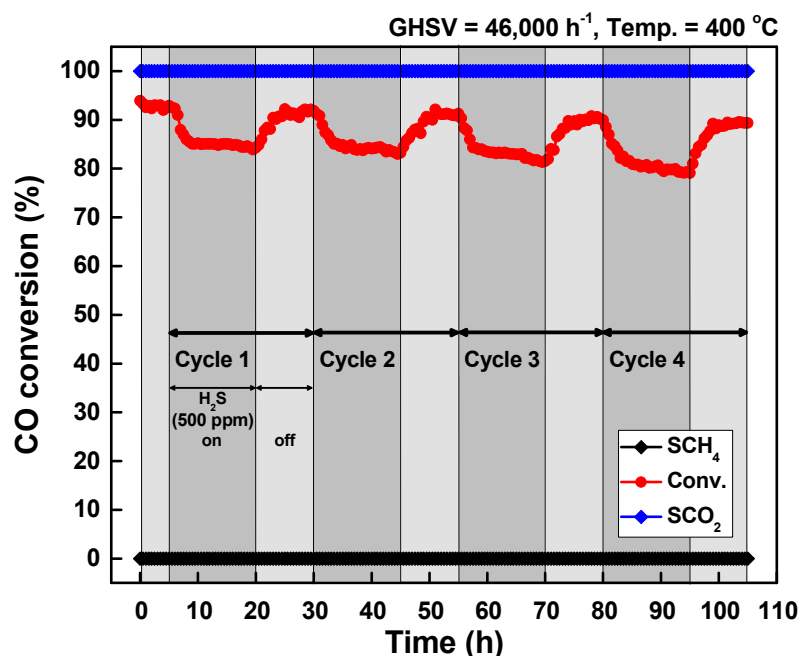


Figure 7. Sulfur-injection shutdown/restart cycle tests over PtCe-I catalyst.

In Figure 8, we summarize the characterization results and the catalytic performance of the CeO₂-supported Pt catalysts prepared by various synthesis methods. The results showed a strong relationship between the physicochemical properties and the catalytic performance of the catalyst. The intrinsic catalytic activity followed the trend of active metal dispersion and, in part, also followed the OSC trend. The OSC of the catalysts affects

sulfur tolerance of the catalyst. The decreased rate of the CO conversion (green color) shows the same trend as the OSC data (blue color) confirmed from H₂-O₂ pulse reaction. As a result, the PtCe-I catalyst shows the highest intrinsic catalytic activity among the prepared catalysts. The PtCe-I catalyst also showed the lowest activity loss and thus the highest sulfur tolerance. As a result, it can be concluded that the active metal dispersion and oxygen-storage capacity of the catalyst are the key factors in the catalytic activity and the sulfur tolerance of the catalyst.

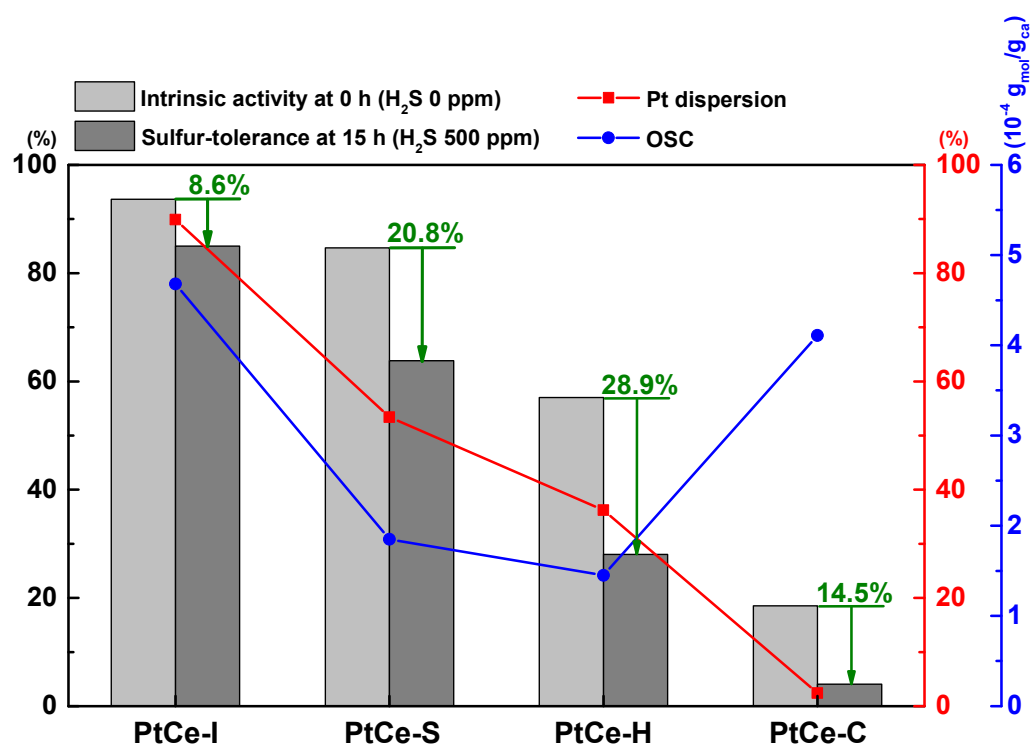


Figure 8. Relationship between the physicochemical properties and the performance of CeO₂-supported Pt catalysts prepared by various synthesis methods.

3. Materials and Methods

3.1. Catalyst Synthesis

CeO₂-supported Pt (98 wt% CeO₂ support, 2 wt% Pt) catalysts were prepared by various synthesis methods (IWI, SG, HT, and CP). For catalyst synthesis, stoichiometrically-calculated Ce(NO₃)₃·6H₂O (99%, Sigma Aldrich, St. Louis, MO, USA) and [Pt(NH₃)₄](NO₃)₂ (50% Pt basis, Sigma Aldrich, St. Louis, MO, USA) were used as precursors. The theoretical Pt loading was fixed at 2 wt%. Table S2 shows the actual Pt content of the catalysts determined by inductively-coupled plasma-optical emission spectrometry (ICP-OES). The details are provided in each section.

3.1.1. Incipient Wetness Impregnation Method

In the case of the PtCe-I catalyst, the pure CeO₂ support was prepared by the precipitation method before the Pt impregnation process. The precursors of Ce were dissolved in deionized water and heated to 80 °C. The mixed solution was treated with dropwise addition of 15 wt% KOH (95%, Samchun Chemicals, Siheung, Republic of Korea) solution until the pH reached 10.5 at 80 °C. Next, the mixture was aged with magnetic stirring for 72 h at 80 °C. The aged solution was washed with deionized water and filtered. The precipitate was dried in an oven overnight at 100 °C and calcined under an air atmosphere at 500 °C in a furnace for 6 h. The Pt precursor dissolved in deionized water (0.5 mL)

was impregnated by dropwise addition into the calcined CeO₂ support. The impregnated mixture was dried and calcined under the same conditions as for pure CeO₂.

3.1.2. Sol-Gel Method

The sol-gel method was used to synthesize the PtCe-S catalyst. Stoichiometric quantities of Pt, Ce precursors, and citric acid were dissolved in 20 mL of deionized water, and the solution was then stirred at 80 °C for 24 h. The gel was formed by citric acid acting as a chelating agent during the slow evaporation of water. The generated gel was heat-treated at 100 °C for 4 h to obtain a swollen mass. This product was then calcined at 500 °C in furnace for 6 h with air.

3.1.3. Hydrothermal Method

To obtain the PtCe-H catalyst, stoichiometric quantities of Pt and Ce precursors were dissolved in 60 mL of deionized water and stirred with a magnetic stirrer at room temperature. After complete dissolution, the pH was adjusted to 10 at 80 °C with an injection of an aqueous 15 wt% NaOH (98%, Daejung Chemicals Co., Pyeongtaek, Republic of Korea) solution. Then, the precipitated solution was heated in a hydrothermal autoclave at 180 °C for 24 h. After this heat treatment, the solution was rinsed and filtered with deionized water to remove impurities. The solid product was dried in an oven overnight at 100 °C and calcined at 500 °C in a furnace for 6 h under an air atmosphere.

3.1.4. Co-Precipitation Method

The PtCe-C catalyst was prepared by the co-precipitation method. The co-precipitation method was carried out using the same process as the precipitation method of the support in the incipient wetness impregnation method section. However, the PtCe-C catalyst was prepared by dissolving the Pt and Ce precursors in deionized water all at once. The mixed solution was heated to 80 °C, and then titration, aging, washing, and filtration processes were sequentially performed. The filtered mixture was then dried and calcined under the conditions described above.

3.2. Catalytic Reaction

The PtCe catalysts prepared by various synthesis methods were tested at 400 °C for evaluation of catalytic performance and sulfur tolerance. A total of 30 mg of catalyst was loaded in a microtubular quartz reactor (I.D. 4 mm). The WGS reaction was performed in a fixed-bed reactor at ambient pressure. Prior to the catalytic test, each catalyst was reduced in situ at 400 °C to form the active phase (PtO_x → Pt⁰). The reactant gas produced through waste gasification consisted of CO (39.70 vol%), CO₂ (21.50 vol%), CH₄ (2.35 vol%), H₂ (27.05 vol%), and N₂ (9.40 vol%). For the WGS reaction, steam was injected at an H₂O/C ratio of 2.0, and the gas hourly space velocity (GHSV) was set to 46,000 h⁻¹. To confirm the catalytic performance in the WGS reaction using waste-derived synthesis gas, the intrinsic catalytic activity of the CeO₂-supported Pt catalysts was evaluated under the above conditions without the injection of sulfur. Then, to account for the sulfur components contained in the waste-derived syngas, a gas containing sulfur was injected. A 1.0% H₂S/Ar gas was injected at a sulfur component ratio of 500 ppm in the total inlet gas. After the WGS reaction, sulfur components and moisture contained in the reaction gas, which cause corrosion and failure of the gas detector, were removed. The compositions of gas products was analyzed by a micro gas analyzer. The detailed procedures and information for the reaction condition such as reaction apparatus, pre-reduction treatment, and sulfur-trapping process after the reaction are reported in our previous work [17]. The CO conversion rate, CO₂ and CH₄ selectivity, and TOF were calculated using the following formulas (Equations (3)–(6)):

$$\text{CO conversion (\%)} = ([\text{CO}]_{\text{in}} - [\text{CO}]_{\text{out}}) / [\text{CO}]_{\text{in}} \times 100 \quad (3)$$

$$\text{CO}_2 \text{ selectivity (\%)} = ([\text{CO}_2]_{\text{out}} - [\text{CO}_2]_{\text{in}}) / (([\text{CH}_4]_{\text{out}} - [\text{CH}_4]_{\text{in}}) + ([\text{CO}_2]_{\text{out}} - [\text{CO}_2]_{\text{in}})) \times 100 \quad (4)$$

$$\text{CH}_4 \text{ selectivity (\%)} = ([\text{CH}_4]_{\text{out}} - [\text{CH}_4]_{\text{in}}) / (([\text{CH}_4]_{\text{out}} - [\text{CH}_4]_{\text{in}}) + ([\text{CO}_2]_{\text{out}} - [\text{CO}_2]_{\text{in}})) \times 100 \quad (5)$$

$$\text{TOF (s}^{-1}\text{)} = (([\text{CO}]_{\text{in}} - [\text{CO}]_{\text{out}}) \times AB_M \times F) / (D \times W \times X_M) \quad (6)$$

where AB_M is the atomic weight of metal (M), F is the total flow rate (mol/s), D is the metal dispersion, W is the mass of catalyst (g), and X_M is the metal content ($g_{\text{metal}}/g_{\text{cat}}$).

3.3. Characterization

The metal concentration of prepared catalysts was analyzed by ICP-OES (IRIS-Thermo Jarrell Ash Co., Waltham, MA, USA). The physicochemical properties of the catalysts were investigated by X-ray diffraction (XRD), Brunauer–Emmett–Teller (BET) analysis, CO pulse chemisorption, H₂-temperature programmed reduction (H₂-TPR), X-ray photoelectron spectroscopy (XPS), H₂-O₂ pulse reaction, Raman spectroscopy, transmission electron microscopy (TEM), and energy dispersive X-ray spectroscopy (EDS). The detailed experimental procedure for all of the above analyses except Raman spectroscopy are mentioned in our previous study [17]. In this study, Raman spectra were recorded using a Horiba Jobin Yvon-LabRam Aramis spectrometer (Longjumeau, France) with a 532 nm excitation line of an Nd-YAG laser.

4. Conclusions

The CeO₂-supported Pt catalysts prepared by various methods were tested for the WGS reaction in a waste-upgrading process. Results showed that the PtCe-I catalyst exhibited the highest Pt dispersion and oxygen-storage capacity. The PtCe-I catalyst also showed superior catalytic activity with high sulfur tolerance compared with the other prepared catalysts. The dispersed Pt on the surface provides a site where CO is adsorbed for a reaction in the redox mechanism of the WGS reaction. The mobile oxygen of the catalyst reacts with CO to promote the WGS reaction and reacts with sulfur to assist the regeneration of the catalytic performance. Through these results, we conclude that the Pt dispersion of the catalyst and the oxygen-storage capacity are important factors for the catalytic performance and sulfur tolerance of the WGS reaction. In conclusion, we found that the optimal catalytic synthesis method is the incipient wetness impregnation method in the CeO₂-supported Pt catalysts for the WGS reaction using waste-derived synthesis gas.

Supplementary Materials: The following supporting information can be downloaded at: <https://www.mdpi.com/article/10.3390/catal12121670/s1>, Figure S1: Adsorption-desorption isotherms of CeO₂-supported Pt catalysts prepared by various synthesis methods; Figure S2: Pore distribution of CeO₂-supported Pt catalysts prepared by various synthesis methods; Figure S3: XPS Pt 4f spectra of poisoned CeO₂-supported Pt catalysts prepared by various synthesis methods; Figure S4: TEM images and particle size distribution results of CeO₂-supported Pt catalysts prepared by various synthesis methods; Figure S5: TEM images and EDS mapping results of poisoned CeO₂-supported Pt catalysts prepared by various synthesis methods; Table S1: Numerical values of catalytic performance at initial (0 h) and poisoned (15 h) points of CeO₂-supported Pt catalysts prepared by various synthesis methods; Table S2: The actual Pt contents of as-synthesized catalysts determined by ICP-OES.

Author Contributions: Conceptualization, G.-R.H. and K.-J.K.; Data curation, G.-R.H., K.-J.K. and Y.-L.L.; Formal analysis, G.-R.H. and K.-J.K.; Funding acquisition, H.-S.R.; Investigation, G.-R.H.; Methodology, S.-Y.A., B.-J.K. and H.-R.P.; Project administration, H.-S.R.; Resources, G.-R.H. and K.-J.K.; Supervision, S.S.L., Y.J. and H.-S.R.; Validation, G.-R.H.; Visualization, G.-R.H.; Writing—original draft, G.-R.H.; Writing—review and editing, G.-R.H., K.-J.K., S.-Y.A., B.-J.K., H.-R.P. and Y.-L.L. All authors have read and agreed to the published version of the manuscript.

Funding: This work was supported by the National Research Foundation of Korea (NRF) grant funded by the Korean government (MSIT) (No. 2020R1A2B5B01002346 and 2022R1A4A1029632). This research was also supported by “Regional Innovation Strategy (RIS)” through the National Research Foundation of Korea (NRF) funded by the Ministry of Education (MOE) (2022RIS-005).

Conflicts of Interest: The authors declare no conflict of interest.

References

1. United Nations, Department of Economic and Social Affairs, Population Division. *World Urbanization Prospects: The 2018 Revision*; United Nations, Department of Economic and Social Affairs, Population Division: New York, NY, USA, 2019.
2. Ozturk, M.; Dincer, I. An Integrated System for Clean Hydrogen Production from Municipal Solid Wastes. *Int. J. Hydrogen Energy* **2021**, *46*, 6251–6261. [[CrossRef](#)]
3. Zheng, X.; Ying, Z.; Wang, B.; Chen, C. Hydrogen and Syngas Production from Municipal Solid Waste (MSW) Gasification via Reusing CO₂. *Appl. Therm. Eng.* **2018**, *144*, 242–247. [[CrossRef](#)]
4. Lee, Y.L.; Lee, K.; Hyun Ko, C.; Roh, H.S. Optimization of Nano-Catalysts for Application in Compact Reformers. *Chem. Eng. J.* **2022**, *431*, 134299. [[CrossRef](#)]
5. Li, S.; Zheng, H.; Zheng, Y.; Tian, J.; Jing, T.; Chang, J.S.; Ho, S.H. Recent Advances in Hydrogen Production by Thermo-Catalytic Conversion of Biomass. *Int. J. Hydrogen Energy* **2019**, *44*, 14266–14278. [[CrossRef](#)]
6. Su, W.; Cai, C.; Liu, P.; Lin, W.; Liang, B.; Zhang, H.; Ma, Z.; Ma, H.; Xing, Y.; Liu, W. Supercritical Water Gasification of Food Waste: Effect of Parameters on Hydrogen Production. *Int. J. Hydrogen Energy* **2020**, *45*, 14744–14755. [[CrossRef](#)]
7. Zhao, J.; Xie, D.; Wang, S.; Zhang, R.; Wu, Z.; Meng, H.; Chen, L.; Wang, T.; Guo, Y. Hydrogen-Rich Syngas Produced from Co-Gasification of Municipal Solid Waste and Wheat Straw in an Oxygen-Enriched Air Fluidized Bed. *Int. J. Hydrogen Energy* **2021**, *46*, 18051–18063. [[CrossRef](#)]
8. Kumar, A.; Samadder, S.R. A Review on Technological Options of Waste to Energy for Effective Management of Municipal Solid Waste. *Waste Manag.* **2017**, *69*, 407–422. [[CrossRef](#)]
9. Lee, Y.L.; Lim, D.; Lee, B.; Upadhyay, M.; Brigljević, B.; Roh, H.S.; Lim, H. Comparative Techno-Economic Analysis of Methanol Production via Carbon Dioxide Reforming of Landfill Gas Using a Highly Active and Stable Nickel-Based Catalyst. *Energy Convers. Manag.* **2022**, *259*, 115585. [[CrossRef](#)]
10. Park, S.W.; Lee, J.S.; Yang, W.S.; Alam, M.T.; Seo, Y.C. A Comparative Study of the Gasification of Solid Refuse Fuel in Downdraft Fixed Bed and Bubbling Fluidized Bed Reactors. *Waste Biomass Valorization* **2020**, *11*, 2345–2356. [[CrossRef](#)]
11. Jang, W.J.; Shim, J.O.; Jeon, K.W.; Na, H.S.; Kim, H.M.; Lee, Y.L.; Roh, H.S.; Jeong, D.W. Design and Scale-up of a Cr-Free Fe-Al-Cu Catalyst for Hydrogen Production from Waste-Derived Synthesis Gas. *Appl. Catal. B* **2019**, *249*, 72–81. [[CrossRef](#)]
12. Renkel, M.F.; Lümmer, N. Supplying Hydrogen Vehicles and Ferries in Western Norway with Locally Produced Hydrogen from Municipal Solid Waste. *Int. J. Hydrogen Energy* **2018**, *43*, 2585–2600. [[CrossRef](#)]
13. Jeong, D.W.; Jang, W.J.; Shim, J.O.; Roh, H.S. High Temperature Water–Gas Shift without Pre-Reduction over Spinel Ferrite Catalysts Synthesized by Glycine Assisted Sol–Gel Combustion Method. *Int. J. Hydrogen Energy* **2016**, *41*, 3870–3876. [[CrossRef](#)]
14. Indrawan, N.; Mohammad, S.; Kumar, A.; Huhnke, R.L. Modeling Low Temperature Plasma Gasification of Municipal Solid Waste. *Environ. Technol. Innov.* **2019**, *15*, 100412. [[CrossRef](#)]
15. Dou, X.; Veksha, A.; Chan, W.P.; Oh, W.D.; Liang, Y.N.; Teoh, F.; Mohamed, D.K.B.; Giannis, A.; Lisak, G.; Lim, T.T. Poisoning Effects of H₂S and HCl on the Naphthalene Steam Reforming and Water-Gas Shift Activities of Ni and Fe Catalysts. *Fuel* **2019**, *241*, 1008–1018. [[CrossRef](#)]
16. Ngo, T.N.L.T.; Chiang, K.Y.; Liu, C.F.; Chang, Y.H.; Wan, H.P. Hydrogen Production Enhancement Using Hot Gas Cleaning System Combined with Prepared Ni-Based Catalyst in Biomass Gasification. *Int. J. Hydrogen Energy* **2021**, *46*, 11269–11283. [[CrossRef](#)]
17. Lee, Y.L.; Kim, K.J.; Hong, G.R.; Ahn, S.Y.; Kim, B.J.; Shim, J.O.; Roh, H.S. Highly Sulfur Tolerant and Regenerable Pt/CeO₂ Catalyst for Waste to Energy. *Renew. Energy* **2021**, *178*, 334–343. [[CrossRef](#)]
18. Lee, Y.L.; Kim, K.J.; Hong, G.R.; Ahn, S.Y.; Kim, B.J.; Park, H.R.; Yun, S.J.; Bae, J.W.; Jeon, B.H.; Roh, H.S. Sulfur-Tolerant Pt/CeO₂ Catalyst with Enhanced Oxygen Storage Capacity by Controlling the Pt Content for the Waste-to-Hydrogen Processes. *ACS Sustain. Chem. Eng.* **2021**, *9*, 15287–15293. [[CrossRef](#)]
19. Lee, Y.L.; Mnoyan, A.; Na, H.S.; Ahn, S.Y.; Kim, K.J.; Shim, J.O.; Lee, K.; Roh, H.S. Comparison of the Effects of the Catalyst Preparation Method and CeO₂ morphology on the Catalytic Activity of Pt/CeO₂ catalysts for the Water-Gas Shift Reaction. *Catal. Sci. Technol.* **2020**, *10*, 6299–6308. [[CrossRef](#)]
20. Pastor-Pérez, L.; Ramos-Fernández, E.V.; Sepúlveda-Escribano, A. Effect of the CeO₂ Synthesis Method on the Behaviour of Pt/CeO₂ Catalysis for the Water-Gas Shift Reaction. *Int. J. Hydrogen Energy* **2019**, *44*, 21837–21846. [[CrossRef](#)]
21. Happel, M.; Mysliveček, J.; Johánek, V.; Dvořák, F.; Stetsovych, O.; Lykhach, Y.; Matolín, V.; Libuda, J. Adsorption Sites, Metal-Support Interactions, and Oxygen Spillover Identified by Vibrational Spectroscopy of Adsorbed CO: A Model Study on Pt/Ceria Catalysts. *J. Catal.* **2012**, *289*, 118–126. [[CrossRef](#)]
22. Zhou, A.; Wang, J.; Wang, H.; Li, H.; Wang, J.; Shen, M. Effect of Active Oxygen on the Performance of Pt/CeO₂ Catalysts for CO Oxidation. *J. Rare Earths* **2018**, *36*, 257–264. [[CrossRef](#)]

23. Puigdollers, A.R.; Schlexer, P.; Tosoni, S.; Pacchioni, G. Increasing Oxide Reducibility: The Role of Metal/Oxide Interfaces in the Formation of Oxygen Vacancies. *ACS Catal.* **2017**, *7*, 6493–6513. [[CrossRef](#)]
24. Lee, J.; Lee, E.; Kim, D.H. Inhibition of Water-Gas Shift Reaction Activity of Oxide-Supported Pt Catalyst by H₂ and CO₂. *Int. J. Hydrogen Energy*, 2022; *in press*. [[CrossRef](#)]
25. Park, Y.M.; Son, M.; Park, M.J.; Bae, J.W. Effects of Pt Precursors on Pt/CeO₂ to Water-Gas Shift (WGS) Reaction Activity with Langmuir-Hinshelwood Model-Based Kinetics. *Int. J. Hydrogen Energy* **2020**, *45*, 26953–26966. [[CrossRef](#)]
26. Li, Y.; Kottwitz, M.; Vincent, J.L.; Enright, M.J.; Liu, Z.; Zhang, L.; Huang, J.; Senanayake, S.D.; Yang, W.C.D.; Crozier, P.A.; et al. Dynamic Structure of Active Sites in Ceria-Supported Pt Catalysts for the Water Gas Shift Reaction. *Nat. Commun.* **2021**, *12*, 914. [[CrossRef](#)]
27. Lee, J.; Shin, D.; Lee, E.; Li, C.; Kim, J.M.; Han, J.W.; Kim, D.H. Alleviating Inhibitory Effect of H₂ on Low-Temperature Water-Gas Shift Reaction Activity of Pt/CeO₂ Catalyst by Forming CeO₂ Nano-Patches on Pt Nano-Particles. *Appl. Catal. B* **2022**, *305*, 121038. [[CrossRef](#)]
28. Zhang, R.; Lu, K.; Zong, L.; Tong, S.; Wang, X.; Zhou, J.; Lu, Z.H.; Feng, G. Control Synthesis of CeO₂ Nanomaterials Supported Gold for Catalytic Oxidation of Carbon Monoxide. *Mol. Catal.* **2017**, *442*, 173–180. [[CrossRef](#)]
29. Kim, K.J.; Lee, Y.L.; Na, H.S.; Ahn, S.Y.; Shim, J.O.; Jeon, B.H.; Roh, H.S. Efficient Waste to Energy Conversion Based on Co-CeO₂ Catalyzed Water-Gas Shift. *Catalysts* **2020**, *10*, 420. [[CrossRef](#)]
30. Li, X.; Li, Y. Influence of the Preparation Method on the Performance of CeO₂-MoO₃ Catalyst for the Selective Catalytic Reduction of NO with NH₃. *React. Kinet. Mech. Catal.* **2014**, *112*, 27–36. [[CrossRef](#)]
31. Lee, Y.L.; Kim, B.J.; Park, H.R.; Ahn, S.Y.; Kim, K.J.; Roh, H.S. Customized Ni-MgO-Al₂O₃ catalyst for Carbon Dioxide Reforming of Coke Oven Gas: Optimization of Preparation Method and Co-Precipitation PH. *J. CO₂ Util.* **2020**, *42*, 101354. [[CrossRef](#)]
32. Wu, S.L.; Kuo, J.H.; Wey, M.Y. Design of Catalysts Comprising a Nickel Core and Ceria Shell for Hydrogen Production from Plastic Waste Gasification: An Integrated Test for Anti-Coking and Catalytic Performance. *Catal. Sci. Technol.* **2020**, *10*, 3975–3984. [[CrossRef](#)]
33. Liu, C.; Zhang, L.; Sun, L.; Wang, W.; Chen, Z. Enhanced Electrocatalytic Activity of PtCu Bimetallic Nanoparticles on CeO₂/Carbon Nanotubes for Methanol Electro-Oxidation. *Int. J. Hydrogen Energy* **2020**, *45*, 8558–8567. [[CrossRef](#)]
34. Mo, L.; Saw, E.T.; Kathiraser, Y.; Ang, M.L.; Kawi, S. Preparation of Highly Dispersed Cu/SiO₂ Doped with CeO₂ and Its Application for High Temperature Water Gas Shift Reaction. *Int. J. Hydrogen Energy* **2018**, *43*, 15891–15897. [[CrossRef](#)]
35. Navarro-Jaén, S.; Romero-Sarria, F.; Centeno, M.A.; Laguna, O.H.; Odriozola, J.A. Phosphate-Type Supports for the Design of WGS Catalysts. *Appl. Catal. B* **2019**, *244*, 853–862. [[CrossRef](#)]
36. Li, F.; Zou, L.; He, J.; Wu, Y.; Yang, L.; Liu, Q.; Wu, Q.; Yang, X. On the Correlation between Structure and Catalytic Activity of Mesoporous Ceria Nanoparticles. *J. Catal.* **2021**, *402*, 300–309. [[CrossRef](#)]
37. Rezaei, M.; Alavi, S.M. Dry Reforming over Mesoporous Nanocrystalline 5% Ni/M-MgAl₂O₄ (M: CeO₂, ZrO₂, La₂O₃) Catalysts. *Int. J. Hydrogen Energy* **2019**, *44*, 16516–16525. [[CrossRef](#)]
38. Lee, J.; Ryou, Y.; Chan, X.; Kim, T.J.; Kim, D.H. How Pt Interacts with CeO₂ under the Reducing and Oxidizing Environments at Elevated Temperature: The Origin of Improved Thermal Stability of Pt/CeO₂ Compared to CeO₂. *J. Phys. Chem. C* **2016**, *120*, 25870–25879. [[CrossRef](#)]
39. Lykhach, Y.; Staudt, T.; Vorokhta, M.; Skála, T.; Johánek, V.; Prince, K.C.; Matolín, V.; Libuda, J. Hydrogen Spillover Monitored by Resonant Photoemission Spectroscopy. *J. Catal.* **2012**, *285*, 6–9. [[CrossRef](#)]
40. Vecchietti, J.; Bonivardi, A.; Xu, W.; Stacchiola, D.; Delgado, J.J.; Calatayud, M.; Collins, S.E. Understanding the Role of Oxygen Vacancies in the Water Gas Shift Reaction on Ceria-Supported Platinum Catalysts. *ACS Catal.* **2014**, *4*, 2088–2096. [[CrossRef](#)]
41. Aranifard, S.; Ammal, S.C.; Heyden, A. On the Importance of Metal-Oxide Interface Sites for the Water-Gas Shift Reaction over Pt/CeO₂ Catalysts. *J. Catal.* **2014**, *309*, 314–324. [[CrossRef](#)]
42. Kim, K.J.; Jeon, K.W.; Hong, G.R.; Jeon, B.H.; Wook Bae, J.; Jang, W.J.; Lee, Y.L.; Roh, H.S. Elucidating the Effect of Ce/Zr Ratio on High Temperature Shift Activity with Sulfur Poisoning. *J. Ind. Eng. Chem.* **2022**, *115*, 537–543. [[CrossRef](#)]
43. Huang, S.; Cheng, B.; Yu, J.; Jiang, C. Hierarchical Pt/MnO₂-Ni(OH)₂ Hybrid Nanoflakes with Enhanced Room-Temperature Formaldehyde Oxidation Activity. *ACS Sustain. Chem. Eng.* **2018**, *6*, 12481–12488. [[CrossRef](#)]
44. Das, S.; Ashok, J.; Bian, Z.; Dewangan, N.; Wai, M.H.; Du, Y.; Borgna, A.; Hidajat, K.; Kawi, S. Silica-Ceria Sandwiched Ni Core-Shell Catalyst for Low Temperature Dry Reforming of Biogas: Coke Resistance and Mechanistic Insights. *Appl. Catal. B* **2018**, *230*, 220–236. [[CrossRef](#)]
45. Liu, B.; Li, C.; Zhang, G.; Yao, X.; Chuang, S.S.C.; Li, Z. Oxygen Vacancy Promoting Dimethyl Carbonate Synthesis from CO₂ and Methanol over Zr-Doped CeO₂ Nanorods. *ACS Catal.* **2018**, *8*, 10446–10456. [[CrossRef](#)]
46. Lee, Y.L.; Jha, A.; Jang, W.J.; Shim, J.O.; Rode, C.V.; Jeon, B.H.; Bae, J.W.; Roh, H.S. Effect of Alkali and Alkaline Earth Metal on Co/CeO₂ Catalyst for the Water-Gas Shift Reaction of Waste Derived Synthesis Gas. *Appl. Catal. A Gen.* **2018**, *551*, 63–70. [[CrossRef](#)]
47. Ahn, S.Y.; Na, H.S.; Jeon, K.W.; Lee, Y.L.; Kim, K.J.; Shim, J.O.; Roh, H.S. Effect of Cu/CeO₂ Catalyst Preparation Methods on Their Characteristics for Low Temperature Water-gas Shift Reaction: A Detailed Study. *Catal. Today* **2020**, *352*, 166–174. [[CrossRef](#)]
48. Artiglia, L.; Orlando, F.; Roy, K.; Kopelent, R.; Safonova, O.; Nachttegaal, M.; Huthwelker, T.; van Bokhoven, J.A. Introducing Time Resolution to Detect Ce³⁺ Catalytically Active Sites at the Pt/CeO₂ Interface through Ambient Pressure X-Ray Photoelectron Spectroscopy. *J. Phys. Chem. Lett.* **2017**, *8*, 102–108. [[CrossRef](#)]
49. Kumar, A.; Sinha, A.S.K. Comparative Study of Hydrogen Production from Steam Reforming of Acetic Acid over Synthesized Catalysts via MOF and Wet Impregnation Methods. *Int. J. Hydrogen Energy* **2020**, *45*, 11512–11526. [[CrossRef](#)]

50. Na, H.S.; Shim, J.O.; Ahn, S.Y.; Jang, W.J.; Jeon, K.W.; Kim, H.M.; Lee, Y.L.; Kim, K.J.; Roh, H.S. Effect of Precipitation Sequence on Physicochemical Properties of CeO₂ Support for Hydrogen Production from Low-Temperature Water-Gas Shift Reaction. *Int. J. Hydrogen Energy* **2018**, *43*, 17718–17725. [[CrossRef](#)]
51. Lee, Y.L.; Kim, B.J.; Park, H.R.; Ahn, S.Y.; Kim, K.J.; Roh, H.S. Improving the Catalytic Activity in Dry Reforming Reaction by Enhancing the Oxygen Storage Capacity of Ce_{0.8}Zr_{0.2}O₂ Support through Hydrogen Heat-Treatment. *J. CO₂ Util.* **2022**, *57*, 101903. [[CrossRef](#)]
52. Jang, W.J.; Shim, J.O.; Kim, H.M.; Yoo, S.Y.; Roh, H.S. A Review on Dry Reforming of Methane in Aspect of Catalytic Properties. *Catal Today* **2019**, 15–26. [[CrossRef](#)]
53. Tepamatr, P.; Laosiripojana, N.; Sesuk, T.; Charojrochkul, S. Effect of Samarium and Praseodymium Addition on Water Gas Shift Performance of Co/CeO₂ Catalysts. *J. Rare Earths* **2020**, *38*, 1201–1206. [[CrossRef](#)]
54. Grabchenko, M.V.; Mamontov, G.V.; Zaikovskii, V.I.; la Parola, V.; Liotta, L.F.; Vodyankina, O.V. The Role of Metal–Support Interaction in Ag/CeO₂ Catalysts for CO and Soot Oxidation. *Appl. Catal. B* **2020**, *260*, 118148. [[CrossRef](#)]
55. Tiwari, S.; Rathore, G.; Patra, N.; Yadav, A.K.; Bhattacharya, D.; Jha, S.N.; Tseng, C.M.; Liu, S.W.; Biring, S.; Sen, S. Oxygen and Cerium Defects Mediated Changes in Structural, Optical and Photoluminescence Properties of Ni Substituted CeO₂. *J. Alloys Compd.* **2019**, *782*, 689–698. [[CrossRef](#)]
56. Kim, B.J.; Seo, J.C.; Kim, D.H.; Lee, Y.L.; Lee, K.; Roh, H.S. Oxygen Defective Bimodal Porous Ni-CeO_{2-x}-MgO-Al₂O₃ Catalyst with Multi-Void Spherical Structure for CO₂ Reforming of CH₄. *J. CO₂ Util.* **2022**, *58*, 101917. [[CrossRef](#)]
57. Lee, Y.L.; Kim, H.Y.; Kim, K.J.; Hong, G.R.; Shim, J.O.; Ju, Y.W.; Roh, H.S. Nanofiber Structured Oxygen Defective CoFe₂O_{4-x} Catalyst for the Water-Gas Shift Reaction in Waste-to-Hydrogen Processes. *Int. J. Hydrogen Energy* **2022**, *47*, 30950–30958. [[CrossRef](#)]